PAPER

Development of interference-free rotational and vibrational thermometry for studies on shock-heated thermochemical non-equilibrium CO

View the article online for updates and enhancements.

Development of interference-free rotational and vibrational thermometry for studies on shock-heated thermochemical non-equilibrium CO

Dong He[1], **Ting Si[1,*]**, **Fei Li[2]** and **Xisheng Luo[1,2]**

[1] Deep Space Exploration Laboratory/Department of Modern Mechanics, University of Science and Technology of China, Hefei 230026, People's Republic of China
[2] State Key Laboratory of High Temperature Gas Dynamics, Institute of Mechanics, Chinese Academy of Sciences, Beijing 100190, People's Republic of China

E-mail: tsi@ustc.edu.cn

CrossMark

Abstract

A mid-infrared interference-free laser absorption technique for simultaneously measuring rotational temperature, vibrational temperature, and CO concentration was developed for application to shock-tube studies on thermochemical non-equilibrium CO over 1000–3000 K. Three transition lines in the fundamental vibrational band of CO (P(0, 21), near 4.87 μm, P(1, 21), near 4.93 μm, and P(0, 37), near 5.05 μm) were selected. The P(0, 21)/P(1, 21) line pair was used for vibrational temperature measurements whereas the P(0, 21)/P(0, 37) line pair was used for rotational temperature measurements. Spectroscopic parameters for developing the technique were measured: line strengths and collisional broadening data in Ar were obtained at 1040–2940 K. Validation experiments for the thermometry system were performed in shock-heated thermal-equilibrium CO/Ar mixtures at 1050–3010 K and 1.1–2.8 bar. The time-dependent rotational and vibrational temperatures were measured during the vibrational relaxation processes of CO. The technique showed high sensitivity in detecting the rotational and vibrational temperatures. The measured rotational temperature agreed well with the temperature calculated using the measured pressure and isentropic relationship. The measured vibrational temperature showed good agreement with the predictions using the Landau and Teller theory and Millikan and White relationship. The time-dependent CO concentration during the oxidation processes of n-heptane over a wide temperature range (1350–2750 K) was measured considering n-heptane as one of the alternative fuels for the scramjet. The interference-free laser absorption strategy showed good flexibility in detecting the CO concentration at ultra-high temperatures. The measured results showed overall good agreement with the predictions from two detailed mechanisms and one skeletal mechanism. The reactivity of n-heptane was found to be insensitive to the temperature increase at ultra-high temperatures (>2100 K).

Supplementary material for this article is available online

(Some figures may appear in colour only in the online journal)

---

* Author to whom any correspondence should be addressed.

1. Introduction

Predicting and managing heat transfer during the entry process is a key prerequisite for deep space exploration. The main component of Martian atmosphere is CO_2. The heat transfer during Mars entry is different from that during Earth reentry. During the Mars entry, the entry velocity is higher than 3 km h^{-1}. The Martian atmosphere in the shock layer is quickly decomposed into CO, O_2, and other species [1]. Johnston *et al* [2] reported that the radiative heating for the Mars Pathfinder probe is significant relative to the convective heating. Cruden *et al* [3] proceeded with absolute radiation measurements in Mars and Venus entry conditions using the NASA Ames' Electric Arc Shock Tube. Cruden *et al* [4] and MacDonald *et al* [5] performed the quantitative measurements of temperature, CO, and CO_2 number densities in the incident-shock-heated environments using the same facility. These studies demonstrated that the CO radiation in CO fourth positive band dominates the overall radiation in the shock layer. Park *et al* [1] developed the kinetics mechanism to describe the thermochemical non-equilibrium states of Martian atmosphere during Mars entry. The two-temperature model was developed to describe the reaction rate coefficients for the Martian atmosphere. Brandis *et al* [6] and Johnston and Brandis [7] reported the corresponding modeling analyses on radiation from the shock-heated high-temperature gases. These studies highlighted that simulations using thermodynamic equilibrium assumptions substantially underpredicted the measured data. Therefore, understanding the real thermodynamic states (e.g., translational, rotational, and vibrational temperatures, simplified as T_{tr}, T_{rot}, and T_{vib}, respectively) of CO_2 and its dissociated products in the shock layer is a key prerequisite to accurately predicting radiation heating.

In addition, online monitoring of temperature and species concentration in combustion is necessary to understand the key processes and optimize the combustor performance. When the Mach number of the hypersonic air-breathing vehicle reaches 6–10, the stagnation temperature in the combustor reaches 2000–5000 K [8]. The combustion chamber works in ultra-high-temperature and extreme-fast-flow environments, which brings tremendous challenges to the highly-selective measurements of target parameters with enough time resolution. CO is a key intermediate during fuel-lean and stoichiometric combustion of hydrocarbons and is a main product during fuel-rich combustion. In addition, the CO concentration in the burnout state is an important indicator for evaluating combustion efficiency. Therefore, developing measurement techniques for accurate temperature and species-concentration measurements in ultra-high-temperature environments is necessary for understanding the transient combustion process in engine combustors. n-Heptane is one of the alternative fuels for the scramjet [9]. The combustion behaviors of n-heptane are well studied considering it is a primary reference fuel for gasoline. Many research

groups developed detailed kinetics mechanisms describing the reaction processes of n-heptane and skeletal mechanisms for utilization in computational fluid dynamics [10–16]. However, at ultra-high temperatures, experimental studies on n-heptane and validation of kinetics mechanisms are still lacking in the literature.

Laser interferometry [17] and gas emission [18] are commonly used methods to measure the vibrational relaxation time of shock-heated thermal non-equilibrium gases. Tunable diode laser absorption spectroscopy (TDLAS) is a highly-selective and non-intrusive technique for simultaneous temperature and species-concentration time-history measurements with microsecond time resolution. Several research groups developed the TDLAS technique for time-resolved measurements of multi-parameters behind shock waves and provided valuable data for studies on chemical non-equilibrium processes including combustion and propulsion [19–23]. In addition, highly-selective measurements of temperature in different freedoms (e.g., rotation and vibration) in the non-equilibrium processes can be achieved by selecting different transition lines of the target species. The Hanson research group at Stanford University has developed the laser absorption technique using transition lines of O_2 and NO and performed quantitative measurements of key parameters during the vibrational excitation and dissociation processes of target species in ultra-high temperature region [24–27]. The transition lines in the fundamental vibrational band of CO distribute in the spectral region of 4.5–5.0 μm. Note that the transition lines of CO_2 and H_2O also distribute in this spectral region. CO_2 and H_2O exist in the atmosphere. In addition, the two species are the main products during hydrocarbon combustion. He *et al* [28] and Mulvihill and Petersen [29] measured the high-temperature absorption cross-section of CO_2 at the centers of CO R-branch lines and subtracted the CO_2 interferences in advance for the measurements in reacting mixtures. However, this approach depends on predicted temperature and CO_2-concentration time histories, which causes additional uncertainties in the measured data. MacDonald *et al* [5] performed CO number density measurements in the shock-heated pure CO environment by selecting the CO R(0, 51) line. Jelloian *et al* [30] developed the translational, rotational, and vibrational thermometry by selecting the R(0, 66), P(0, 31), P(2, 20), and P(3, 14) lines in the fundamental vibrational band of CO. However, broadband interferences of CO_2 absorbances are observed at the centers of R(0, 51) and R(0, 66) lines, which limits the flexibility of highly-selective measurements in CO_2-enriched environments.

The kinetics shock tube is an ideal high-temperature facility for studies on high-temperature spectroscopy and thermochemical non-equilibrium gas kinetics. Several groups [31–35] performed high-temperature spectrum calibration behind reflected shock waves to obtain the parameters including the line strength, collisional broadening coefficient, and absorption cross-section. Studies on the vibrational excitation and decomposition of high-temperature gases

were also reported using the shock-tube facility [24–27, 36]. However, for the measurements of thermochemical non-equilibrium CO, selecting specific transition lines and calibrating the spectral parameters at elevated temperatures is necessary.

In this study, a mid-infrared interference-free TDLAS technique was developed for simultaneous measurements of time-resolved T_{rot}, T_{vib}, and CO concentration for studies on the shock-heated thermochemical non-equilibrium CO. Firstly, the transition lines in the fundamental vibrational band of CO, P($v'' = 0$, $J'' = 21$), P($v'' = 1$, $J'' = 21$), and P($v'' = 0$, $J'' = 37$), were selected to develop the interference-free laser absorption technique. These lines were simplified as P(0, 21), P(1, 21), and P(0, 37) in the following part. The P(0, 21)/P(1, 21) line pair was used for T_{vib} measurements whereas the P(0, 21)/P(0, 37) line pair was used for T_{rot} measurements. The temperature-dependent line strengths and collisional broadening coefficients in Ar were measured to develop the laser-absorption system considering the spectroscopic parameters are still lacking in the literature. The technique was subsequently demonstrated by measuring temperature and CO concentration in shock-heated thermal equilibrium nonreactive mixtures. The technique was then applied to temperature and CO concentration measurements during the vibrational relaxation processes of shock-heated CO/Ar mixture and the oxidation processes of $nC_7H_{16}/O_2/Ar$ mixtures. The measured data were compared with predictions from the corresponding models to validate the selectivity and feasibility of the proposed technique. Additionally, the measured data from reactive $nC_7H_{16}/O_2/Ar$ mixtures were used to show the reactivity of n-heptane over a wide temperature range.

2. TDLAS

2.1. Theory

This section briefly introduces the basic theory of TDLAS [20]. When a narrow bandwidth laser beam transmits through a uniform gas medium, the intensity of the incident beam follows the Beer–Lambert law as described in equation (1)

$$I_t/I_0 = \exp\left[-pS_{ji}(T)xL\varphi(v_{ji})\right] = \exp\left[-\alpha(v_{ji})\right] \quad (1)$$

with the transmitted beam intensity I_t, the pressure p, the line strength at a given temperature $S_{ji}(T)$, the mole fraction of the target species x, the optical path L, the line center of the target transition v_{ji}, the line shape function $\varphi(v_{ji})$ (here: Voigt), and the absorbance $\alpha(v_{ji})$. In the thermal equilibrium state, the temperature-dependent line strength is described as follows:

$$S_{ji}(T) = S_{ji}(T_0)\frac{Q(T_0)}{Q(T)}\frac{T_0}{T}\exp\left[-\frac{hcE''}{k_B}\left(\frac{1}{T} - \frac{1}{T_0}\right)\right]$$
$$\times \left[1 - \exp\left(\frac{-hcv_{ji}}{k_BT}\right)\right]\left[1 - \exp\left(\frac{-hcv_{ji}}{k_BT_0}\right)\right]^{-1} \quad (2)$$

with the reference temperature T_0, the partition function Q, the lower-state energy E'', the Planck constant h, the light speed c, and the Boltzmann constant k_B. Temperature measurements are obtained by the ratiometric method as described in equation (3),

$$R = \frac{[\alpha(v_{ji})]_1}{[\alpha(v_{ji})]_2} = \frac{[S_{ji}(T)\varphi(v_{ji})]_1}{[S_{ji}(T)\varphi(v_{ji})]_2}. \quad (3)$$

The full-width at half maximum of the collisional broadening, δv_c, is described as follows:

$$\delta v_c = p\left(\sum_k x_k \times 2\gamma_k(T_0)\left(\frac{T_0}{T}\right)^{n_k}\right) \quad (4)$$

with the mole fraction of the collision partner x_k, the room-temperature collisional broadening coefficient $2\gamma_k(T_0)$, and the corresponding temperature exponent n_k. $2\gamma_k(T_0)$ and n_k depend on the specific collision partner. Therefore, measuring the correct collisional information for the target collision partner is necessary.

In the thermal-equilibrium state, $S_{ji}(T)$ can also be described as follows:

$$S_{ji}(T) = I_a\frac{A_{ji}}{8\pi cv_{ji}^2}\frac{g'\exp\left(-\frac{hcE''}{k_BT}\right)\left[1 - \exp\left(-\frac{hcv_{ji}}{k_BT}\right)\right]}{Q(T)} \quad (5)$$

with the natural terrestrial isotopic abundance I_a, the Einstein coefficient A_{ji}, and the upper state statistical weight g'. The above-mentioned parameters can be inferred directly from the most recent HITEMP database [37]. In thermal non-equilibrium processes, the translational mode and rotational mode of the gas molecule can easily reach an equilibrium state, whereas the vibrational mode needs many collisions before it becomes vibrationally excited. Therefore, the translational and rotational energies are assumed to follow the Boltzmann distribution with the same temperature ($T_{tr} = T_{rot}$), whereas the vibrational energy independently follows the Boltzmann distribution with T_{vib}. The definition of line strength accounting for T_{rot}, T_{vib}, lower-state energies, and transition energy changes is shown in equation (6)

$$S_{ji}\left(T_{rot}, T_{vib}\right) = I_a \frac{A_{ji}}{8\pi c v_{ji}^2} \frac{g' \exp\left[-\frac{hc}{k_B}\left(\frac{E_{rot}''}{T_{rot}} + \frac{E_{vib}''}{T_{vib}}\right)\right]\left\{1 - \exp\left[-\frac{hc}{k_B}\left(\frac{\Delta E_{rot}}{T_{rot}} + \frac{\Delta E_{vib}}{T_{vib}}\right)\right]\right\}}{Q_{rot}\left(T_{rot}\right)Q_{vib}\left(T_{vib}\right)} \quad (6)$$

where $Q_{rot}(T_{rot})$ and $Q_{vib}(T_{vib})$ are the rotational and vibrational partition functions, respectively; E_{rot}'' and E_{vib}'' are the rotational and vibrational lower-state energies, respectively; ΔE_{rot} and ΔE_{vib} are the rotational and vibrational transition energy changes, respectively. Therefore, selecting the line pair with its line-strength ratio sensitive to T_{rot} and selecting the line pair with its line-strength ratio sensitive to T_{vib} are prerequisites to performing highly-selective and accurate measurements of T_{rot} and T_{vib}.

Note that in the thermal non-equilibrium process, the translational mode and rotational mode of CO quickly reach an equilibrium state. This is also validated in figure 12. Therefore, T_{rot} was used to describe the Voigt line shape function for the selected lines.

2.2. Line selection

Three transition lines in the CO fundamental vibrational band, P(0, 21), P(1, 21), and P(0, 37), were selected to develop the TDLAS system considering the limited optical path. The detailed spectral information of the selected lines are shown in table 1. The P(0, 21)/P(0, 37) line pair was used for T_{rot} measurement while the P(0, 21)/P(1, 21) line pair was used for T_{vib} measurement. Temperature sensitivity defined as equation (7) is a key parameter limiting the upper temperature range of the ratiometric method. Note that the temperature sensitivity should be higher than unity in the target temperature range to ensure sensitive temperature measurements. The line strength, temperature sensitivity, and line-strength ratio of the selected line pairs are shown in figure 1. The temperature sensitivity of the P(0, 21)/P(0, 37) line pair is higher than unity in 1000–2600 K, whereas that of the P(0, 21)/P(1, 21) line pair is higher than unity in 1000–3000 K. The difference in the lower-state energy of the selected line pair limits the upper limit of temperature measurement for the current method,

$$\frac{(dS_{ji}/S_{ji})}{(dT/T)} \approx \frac{hc}{k} \frac{|E_2'' - E_1''|}{T}. \quad (7)$$

The spectral lines in the fundamental vibrational band of CO distribute in the spectral range of 4.5–5.0 μm. However, in this wavelength range, transition lines of CO_2 and H_2O are observed at room and elevated temperatures, as shown in figure 2. CO_2 and H_2O widely exist in the atmosphere and the two species are the main products during hydrocarbon combustion. In addition, the experiments simulating Mars entry are performed in CO_2-enriched environment. The absorbance

interferences from CO_2 and/or H_2O inevitably bring additional uncertainties to the measured results and limit the availability of the TDLAS technique. Therefore, the absorbances of CO_2 and H_2O were calculated at room and elevated temperatures, as shown in figure 3. For room-temperature case: $p = 1.0$ bar, $T = 300$ K, $L = 200.0$ cm, $x_{CO2} = 400$ ppm, and $x_{H2O} = 2.0\%$. For high-temperature case: $p = 3.0$ bar, $T = 2000$ K, $L = 10.0$ cm, $x_{CO} = 1.0\%$, $x_{CO2} = 10.0\%$, and $x_{H2O} = 10.0\%$. At the line center of the P(0, 37) line, the absorbance interferences of CO_2 and H_2O are negligible. The corresponding absorbance calculations for P(0, 21) and P(1, 21) lines are referred to in the previous study [39] (here these profiles are shown in supplemental material S1). Therefore, the absorbance interferences of the two species can be neglected in the data processing procedure in section 4.

This study simulated the line-strength ratios of P(0, 21)/P(0, 37) and P(0, 21)/P(1, 21) line pairs as a function of T_{rot} and T_{vib} in 1000–3000 K, as shown in figure 4. In the target temperature range, the line-strength ratio of P(0, 21)/P(0, 37) line pair showed strong dependence on T_{rot} whereas the line-strength ratio of P(0, 21)/P(1, 21) line pair showed strong dependence on T_{vib}. Therefore, the selected line pairs can achieve highly-selective measurements on T_{rot} and T_{vib}.

3. Experiments

3.1. Shock tube facility

Experiments were performed in a kinetics shock tube with an inner diameter of 10.07 cm, a driver section of 3.3 m, and a driven section of 6.4 m [39]. Polyethylene terephthalate diaphragms were used to divide the driver and driven section. Helium was used as the driver gas. Four pressure transducers (PCB 113B26) installed in the sidewall of the driven section were used to measure the velocity of the incident shock. The velocity of the incident shock at the endwall was calculated through extrapolation. The temperature (T_5) and pressure (p_5) behind reflected shock waves were calculated based on the one-dimensional shock-wave equation. The uncertainties in T_5 and p_5 are around 1.0% and 1.5%, respectively. For the non-equilibrium process of CO, the T_5 and p_5 were calculated assuming that CO is in a vibrational frozen state. All transducers were coated with a thin layer of silicon components (RTV 106) to shield them from heat transfer and gas ionization. One of the transducers was installed 20 mm from the endwall to measure the time-resolved pressure profiles. Two opposing CaF_2 windows were installed at the same cross-section for TDLAS measurements. The windows were wedged at 3° to avoid unwanted beam

Table 1. Spectral information of CO transition lines. Reprinted from [38], Copyright (2022), with permission from Elsevier.

Transitions (v'', J'')	Wavenumber (cm^{-1})	Wavelength (nm)	Lower-state energy (cm^{-1})
P(0, 21)	2055.40	4865.23	886.90
P(1, 21)	2029.66	4926.93	3022.09
P(0, 37)	1978.93	5053.24	2690.99
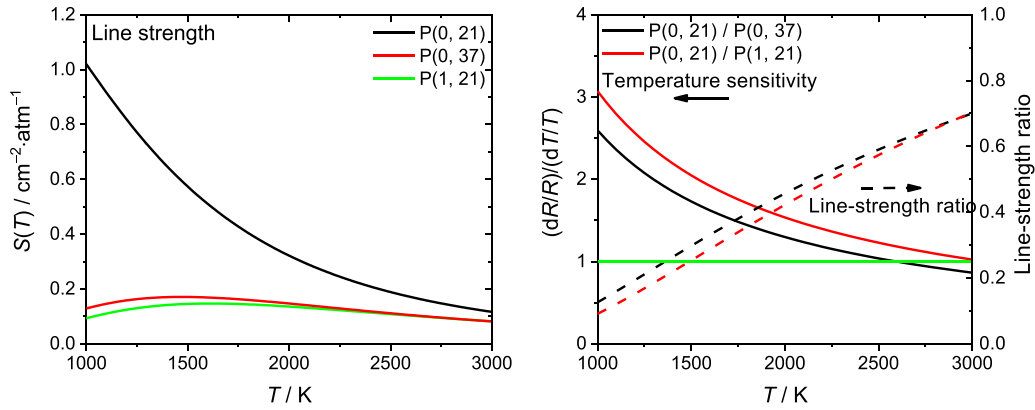
Figure 1. Line strengths, temperature sensitivities, and line-strength ratios for line pairs of CO P(0, 21)/P(0, 37) and P(0, 21)/P(1, 21). Data from the HITEMP [37] database were used here.
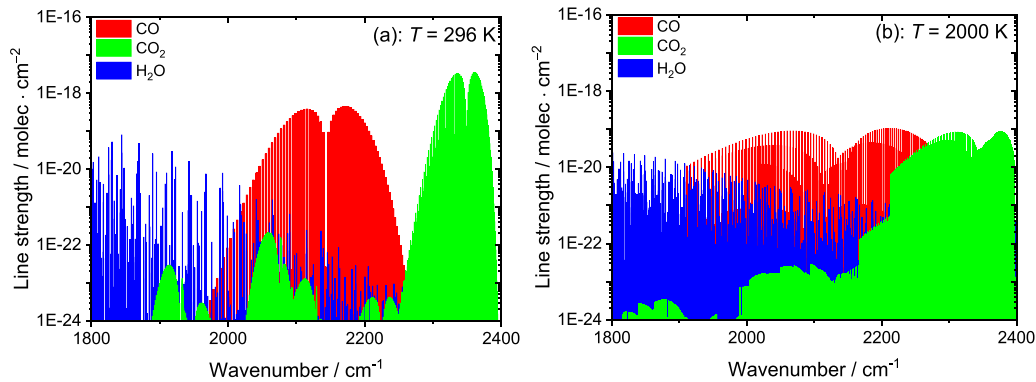
Figure 2. Spectral lines of CO, CO_2, and H_2O in the fundamental vibrational band of CO. Data from the HITEMP [37] database were used here.

interferences. The leakage rate of the shock tube is lower than 2.3×10^{-3} Pa min^{-1}.

Table 2 shows the detailed mixture compositions and experimental conditions in this study. All mixtures were prepared in a 50.24 l mixture vessel based on Dalton's law of partial pressure and rested for at least 12 h before use to ensure homogeneity. The double dilution method was used to prepare the species with mole fractions lower than 1.0%. Mixture 1 was used for measurements of high-temperature spectral parameters of P(0, 21) in 2000–3000 K. Mixture 2 was used for measurements of high-temperature spectral parameters of P(1, 21) in 2000–3000 K and P(0, 37) in 1000–3000 K. Mixture 3 was used to measure temperature and CO-concentration time histories behind reflected shock waves and to validate the accuracy of the selected line pairs. The added H_2 was used to accelerate the vibrational relaxation process of CO.

Mixture 4 was used for simultaneous T_{rot} and T_{vib} measurements in the shock-heated thermal non-equilibrium CO/Ar mixture. Mixtures 5 and 6 were used for time-resolved CO-concentration measurements during the oxidation processes of nC_7H_{16} at equivalence ratios of 2.0 and 1.0 over a wide temperature range. To reduce the effect of potential adsorption gas on the high-temperature experiments, the test mixtures were used to wash and clean the inner surface of the driven section before each shock.

Matthews [40] emphasized that H_2O showed an evident reduction on the vibration relaxation time of CO due to the near-resonant transfer of vibrational energy between CO and H_2O molecules. von Rosenberg *et al* [41] measured and summarized $p\tau$(CO-H_2O) as 0.17 atm·μsec in 1230–2600 K. Therefore, for mixture 4, the purity of Ar reaches 99.9999% with H_2O lower than 400 ppb (Air Liquide). He *et al* [21]
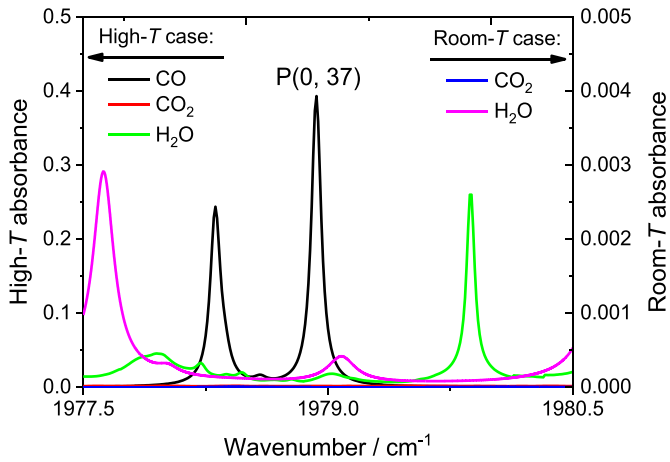
Figure 3. Simulated CO spectra and interferences of CO_2 and H_2O absorbances. High-T case: $p = 3.0$ bar, $T = 2000$ K, $L = 10.0$ cm, $x_{CO} = 1.0\%$, $x_{CO2} = 10.0\%$, and $x_{H2O} = 10.0\%$. Room-T case: $p = 1.0$ bar, $T = 300$ K, $L = 200.0$ cm, $x_{CO2} = 400$ ppm, and $x_{H2O} = 2.0\%$. Data from the HITEMP [37] database were used here.
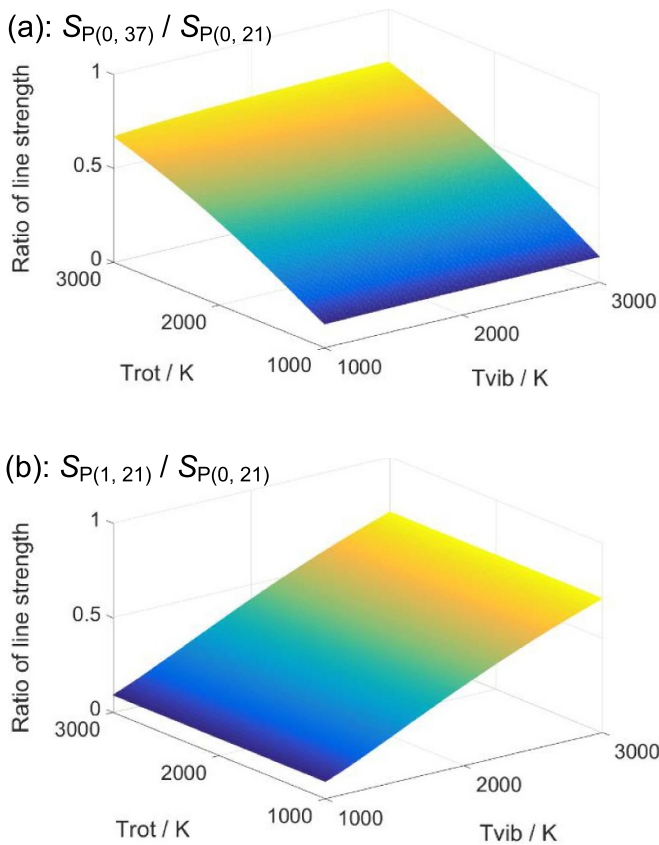

Figure 4. Simulated line-strength ratios as a function of T_{rot} and T_{vib}. (a): P(0, 37)/P(0, 21) line pair. (b): P(1, 21)/P(0, 21) line pair. Data from the HITEMP [37] database were used here.

reported that the formed CO during the pyrolysis of oxygenated hydrocarbons relaxed towards thermal equilibrium very quickly due to the contribution of formed H_2. Therefore, for mixtures 5 and 6, the formed CO was assumed to quickly reach a thermal equilibrium state.

3.2. Laser absorption setup

A TDLAS setup was developed for simultaneous T_{rot}, T_{vib}, and CO-concentration time-history measurements behind reflected shock waves, as shown in figure 5. The schematic was divided into the laser part, the detection part, and the wavelength-calibration part. In the laser part, three interband cascade lasers (Nanoplus) were used to access the P(0, 21) line near 4.87 μm, the P(1, 21) line near 4.93 μm, and the P(0, 37) line near 5.05 μm. The three lasers were controlled by three laser controllers (Arroyo instrument, 6305, combining the thermoelectric cooler and current elements). The laser beams were focused into the shock tube by a concave mirror. In the detection part, three mid-IR detectors were used to detect the corresponding laser beams. Three bandpass filters (Hangzhou Multi IR Technology, INBP–4870–220 nm; Spectrogon, BP–4950–200 nm and NB–5040–155 nm) were fixed in front of the detectors to diminish thermal emission. The fixed-wavelength direct-absorption method was used to ensure the measurement time resolution of 1 μs. Therefore, in the wavelength-calibration part, a 33.8 cm single-pass cell and a 23.56 m Herriot cell were used to position the wavelength of the lasers on the centers of the target lines. The optical elements corresponding to the P(0, 37) line (laser and detector) were coupled into our previous TDLAS setup [39]. The wavelengths of the selected lines were close to one another. Using commercial (narrow) bandpass filters to separate the colinear beams is difficult. Therefore, the cross-beam method was used to ensure the selective detection of beams from the respective laser only.

The scanned-wavelength direct-absorption method was used to measure the spectral parameters of the three transition lines at elevated temperatures. A function generator (Keysight 33510B) was connected to the laser controller to generate a sinusoidal current with a frequency of 2.0 kHz. A 76.2 mm germanium etalon with a free spectral range of 0.016 cm^{-1} was used to convert the absorbance feature from the time domain into the frequency domain. Detailed results and calibrated spectral information were shown in section 5.1. Note that the hot region behind reflected shock waves is not temporally invariant constant due to the non-ideal effects inside the shock tube. Therefore, during the calibration process, the temperature was calculated based on T_5, p_5, measured pressure, and isentropic relationship.

The relative vibrational amplitudes of the three laser beams were all lower than 0.2% in one shock. The experiments with the lasers switched off showed that the relative amplitudes of thermal emission were all below 0.4% at 2962 K and 1.3 bar for the three detectors in figure 5. Therefore, the effects of beam vibration and gas emission were neglected in this study. The detailed results are shown in supplemental material S2.

4. Data processing procedure

An iterative process was used to automatically calculate the T_{rot}, T_{vib}, and CO concentration (x_{CO}) for the shock-heated thermal non-equilibrium mixture (mixture 4) at each time point behind reflected shock waves, as shown in figure 6. The

Table 2. Mixture compositions and experimental conditions.

Mixture#	CO, mol%	H_2, mol%	nC_7H_{16}, mol%	O_2, mol%	Ar, mol%	p/bar	T/K	ϕ
1	1.0	2.0	—	—	97.0	$\sim$1.2	2100–2920	—
2	1.5	2.0	—	—	96.5	$\sim$1.2	1040–2940	—
3	1.0	2.0	—	—	97.0	1.1–2.8	1050–3010	—
4	1.0	—	—	—	99.0	2.1	1846	—
5	—	—	0.06	0.33	99.61	1.6–2.3	1510–2750	2.0
6	—	—	0.06	0.66	99.28	1.7–2.5	1350–2380	1.0
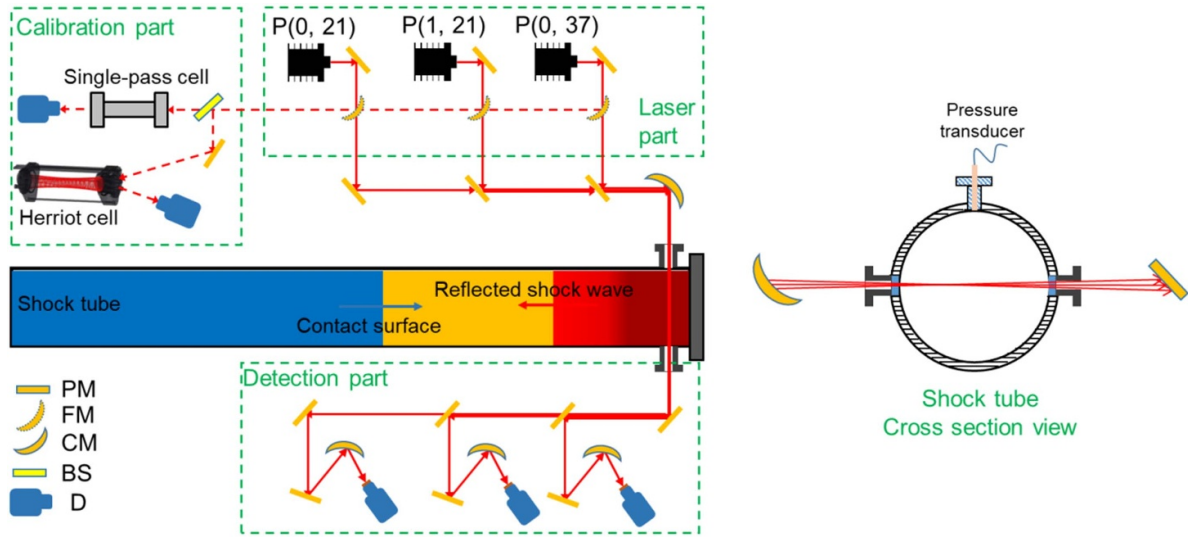
Figure 5. Schematic diagram of the laser absorption setup. (PM: plane mirror; FM: flip mirror; CM: concave mirror; BS: beam splitter; D: detector).

I_0, I_t, and measured pressure were used as inputs. For each time point, initial T_{rot}, T_{vib}, and x_{CO} were assumed to start the iterative process. Then, the code calculated a new rotational temperature (T'_{rot}) and a new vibrational temperature (T'_{vib}) based on the absorbance ratios of P(0, 21)/P(0, 37) and P(0, 21)/P(1, 21) line pairs, respectively. The code subsequently calculated a new CO concentration (x'_{CO}) based on equation (6). If the deviations between T_{rot} and T'_{rot}, T_{vib} and T'_{vib}, and x_{CO} and x'_{CO} are all acceptable, the code records the data and passes to the next time step. Note that the line-shape function is related to the thermal motion of gas molecules. Therefore, T_{rot} was used to calculate the line-shape function.

The Landau–Teller theory [42] was used to describe the time-dependent vibrational energy of shock-heated molecules, as described in equation (8)

$$\frac{de_{vib}}{dt} = \frac{\bar{e}_{vib}(T_{tr}) - e_{vib}(T_{vib})}{\tau(T_{tr})} \tag{8}$$

where e_{vib} is the vibrational energy, $\bar{e}_{vib}(T_{tr})$ is the equilibrium value of vibrational energy, and τ is the vibrational relaxation time. The vibrational energy of CO is calculated based on equation (9) assuming CO as a simple harmonic oscillator

$$e_{vib} = \frac{\theta_{vib}/T_{vib}}{e^{\theta_{vib}/T_{vib}} - 1} RT_{vib} \tag{9}$$

where θ_{vib} is the characteristic vibrational temperature of CO and R is the universal gas constant. The time-dependent T_{rot} ($=T_{tr}$) and T_{vib} were calculated using the theory developed by Landau and Teller [42] and the vibrational relaxation times summarized by Millikan and White [43].

The simultaneous temperature and CO-concentration measurements were performed during the oxidation processes of nC_7H_{16}/O_2/Ar mixtures at 1350–2750 K, 1.6–2.7 bar, and equivalence ratios of 2.0 and 1.0. The measured data were used to show the overall formation and consumption behaviors of chemical non-equilibrium CO and to show the reactivity of n-heptane over a wide temperature range. The measured data were compared with predictions based on the NUIGMech1.1 [10, 11], the CRECK [12–15] mechanism, and the Liu *et al* [16] mechanism to comprehensively evaluate the performances of these mechanisms. The NUIGMech1.1 [10, 11] contains 2746 species and 11 279 elementary reactions. The n-heptane sub-mechanism in NUIGMech1.1 [10, 11] was updated based on Zhang *et al* [44, 45]. The CRECK [12–15] mechanism contains 254 species and 7568 reactions. Liu *et al* [16] developed a skeletal methanol/n-heptane mechanism including 52 species and 182 reactions for three-dimensional simulations. In addition, during ignition, the assumption of constant volume or constant pressure is not valid anymore due to the non-ideal effects inside shock tubes and heat exchange. Therefore, the measured pressure was used as input during kinetics calculation to diminish the gaps between experiments
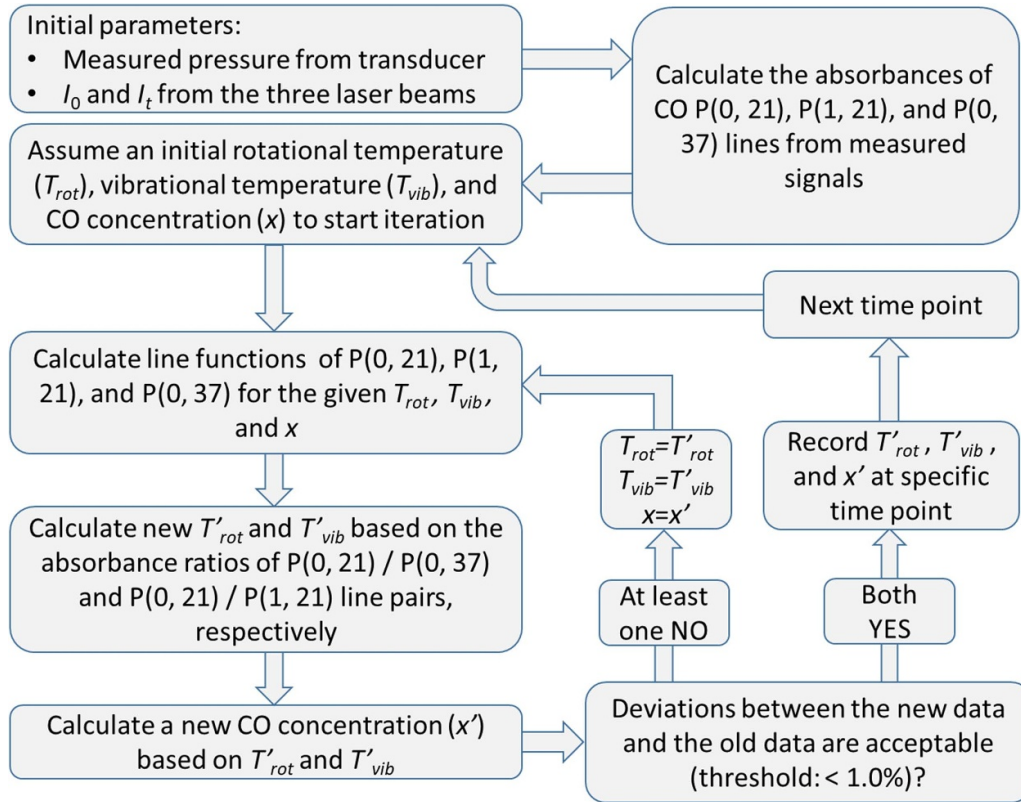
Figure 6. Iterative process for simultaneous T_{rot}, T_{vib}, and CO-concentration calculation.

and simulations. Details about this method are referred to [28, 31, 46].

5. Results and discussion

5.1. Spectral information and validation experiments

The temperature-dependent line strengths and collisional broadening coefficients are necessary inputs during data processing. Note that the spectral parameters of most lines lack calibration research at elevated temperatures. Therefore, the scanned-wavelength direct-absorption method was used to calibrate the line strengths and collisional broadening coefficients of the selected lines. Figure 7 shows an example in a one-shock experiment, including I_0, I_t, the transmitted beam intensity through the Herriot cell I_{cell}, the transmitted beam intensity through the germanium etalon I_{etalon}, the absorbance of P(1, 21) line at specific temperature and pressure, and the fitting residual. Considering the non-ideal effects inside the shock tube, the temperature corresponding to the absorbance region was calculated based on T_5, p_5, the measured pressure, and the isentropic relationship.

The measured line strengths and collisional data of the selected lines were measured at 1040–2940 K and summarized in figure 8. In the target temperature range, the measured line strengths of P(0, 21) line fitted well with the data in the latest HITEMP database [37, 47], whereas the measured data of P(1, 21) line fitted well with the data in HITRAN 2020 database [38]. Therefore, the parameters in the corresponding

spectral database were used in the data processing procedure. The measured line strengths of P(0, 37) did not fit well with the data in either the HITRAN 2020 database [38] or the HITEMP database [37]. Therefore, the fitted data were used. The measured collisional data of the selected lines were fitted as an exponential function of temperature, as shown in figure 8(b). The calibrated spectral information of the selected lines are shown in table 3. Note that the collisional data of P(0, 21) and P(1, 21) lines in this study are slightly different from the data in the previous study [39] due to the fitting temperature range (Here the previously calibrated data are shown in supplemental material S3). However, in the 1000–2000 K temperature range, the differences in the collisional data were negligible.

The temperature and CO-concentration measurements were performed behind reflected shock waves at 1.1–2.8 bar to evaluate the accuracy of the P(0, 21)/P(1, 21) line pair and the P(0, 21)/P(0, 37) line pair, as shown in figure 9. The validation temperature range for the former line pair is 1050–3010 K, whereas that for the latter is 1050–2540 K considering its relatively low temperature sensitivity. The validation experiments demonstrated that the maximum deviation between the measured and calculated data (temperature and CO concentration) is below 1.8% and 3.0%, respectively.

This section mainly focuses on the uncertainties in measured T_{rot} and T_{vib}. The results in figure 4 illustrated that the line-strength ratio of the CO P(0, 21)/P(1, 21) line pair is T_{vib}-dependent, where that of the CO P(0, 21)/P(0, 37) line pair is T_{rot}-dependent. Therefore, for uncertainty evaluation in the thermal non-equilibrium process, the following were assumed:
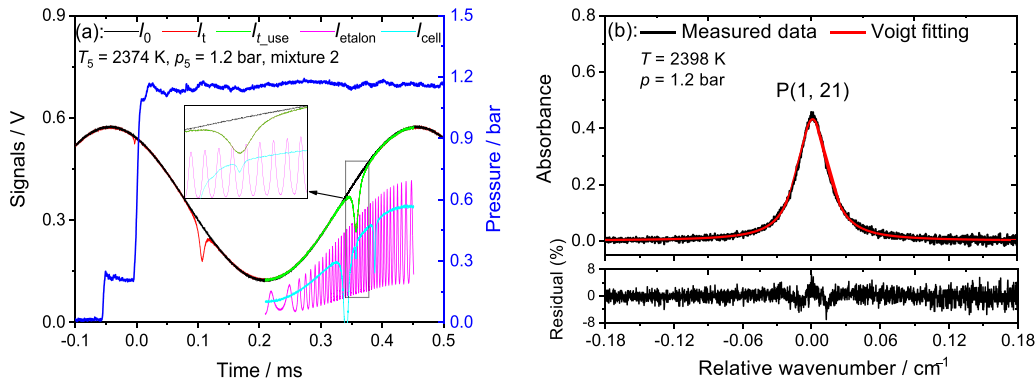
Figure 7. (a): Measured raw data of the CO P(1, 21) line when scanning the laser. (b): The absorbance of the P(1, 21) line, the Voigt fitting, and the fitting residual for the case.
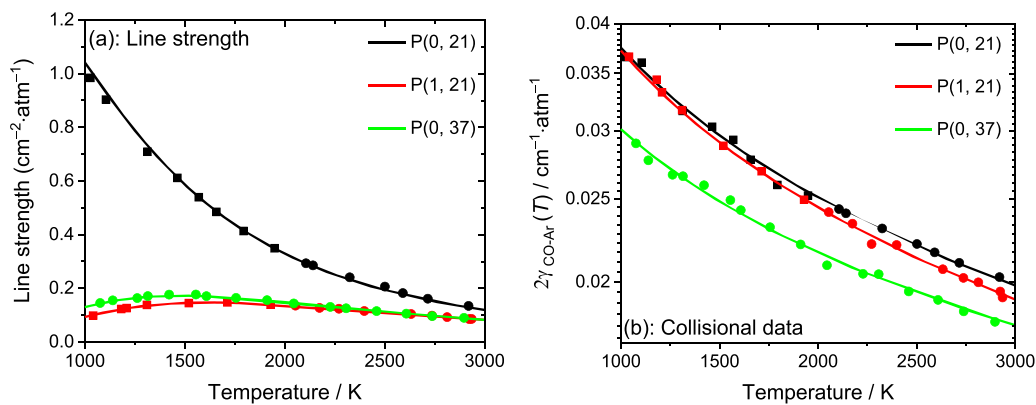

Figure 8. (a): Measured and fitted line strengths of CO P(0, 21), P(1, 21), and P(0, 37) lines at elevated temperatures. (b): Corresponding collisional broadening coefficients $2\gamma_{CO\text{-}Ar}$ for the three transitions. Square (■ ■): the data from the previous study [39]. Round (● ● ●): the data measured in this study.

Table 3. Calibrated spectral parameters for the selected lines.

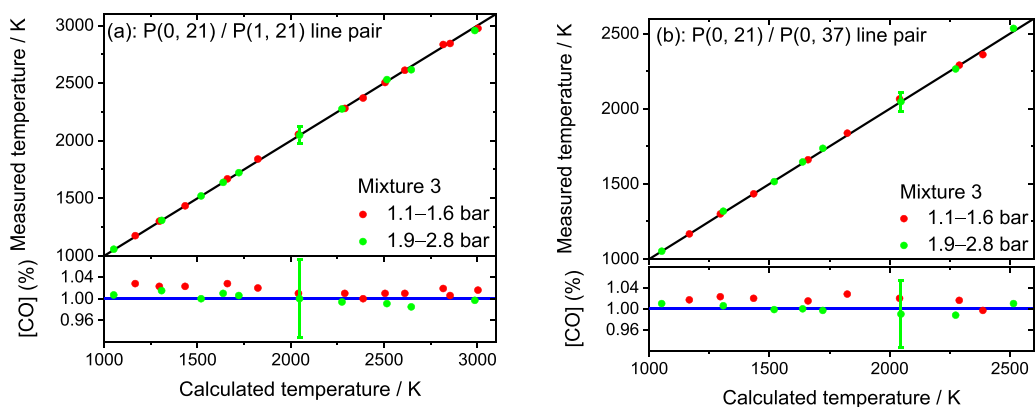| Transition	S(296 K) (cm^{-2}·atm^{-1})		$2\gamma_{CO\_Ar}$ (296 K) (cm^{-1}·atm^{-1})	n
(v'', J'')	Data	Sources	Data fitted to 1040–2940 K	Data fitted to 1040–2940 K
P(0, 21)	0.633	HITEMP [37, 47]	0.0761 ± 0.0014	0.581 ± 0.011
P(1, 21)	3.81×10^{-5}	HITRAN 2020 [38]	0.0780 ± 0.0009	0.608 ± 0.006
P(0, 37)	1.65×10^{-5}	Fitting	0.0540 ± 0.0010	0.479 ± 0.011

Figure 9. Temperature and CO-concentration measurements (validation experiments) at various temperatures and pressures for (a): P(0, 21)/P(1, 21) line pair and (b): P(0, 21)/P(0, 37) line pair.

$$R_{Tvib} = \frac{\alpha_{P(0,21)}}{\alpha_{P(1,21)}} = \frac{[pS_{ji}(T_{rot}, T_{vib})xL\varphi(T_{rot})]_{P(0,21)}}{[pS_{ji}(T_{rot}, T_{vib})xL\varphi(T_{rot})]_{P(1,21)}} \approx \frac{[S_{ji}(T_0)\varphi(T_{rot})]_{P(0,21)}}{[S_{ji}(T_0)\varphi(T_{rot})]_{P(1,21)}} \exp\left[-\frac{hc}{k_B}\left(\frac{E''_{vib,P(0,21)}}{T_{vib}} - \frac{E''_{vib,P(1,21)}}{T_{vib}}\right)\right] \quad (10)$$

$$R_{Trot} = \frac{\alpha_{P(0,21)}}{\alpha_{P(0,37)}} = \frac{[pS_{ji}(T_{rot}, T_{vib})xL\varphi(T_{rot})]_{P(0,21)}}{[pS_{ji}(T_{rot}, T_{vib})xL\varphi(T_{rot})]_{P(0,37)}} \approx \frac{[S_{ji}(T_0)\varphi(T_{rot})]_{P(0,21)}}{[S_{ji}(T_0)\varphi(T_{rot})]_{P(0,37)}} \exp\left[-\frac{hc}{k_B}\left(\frac{E''_{rot,P(0,21)}}{T_{rot}} - \frac{E''_{rot,P(0,37)}}{T_{rot}}\right)\right]. \quad (11)$$

Therefore, the uncertainties in measured T_{rot} and T_{vib} are mainly from the uncertainties in room-temperature line strengths and measured absorbances. The uncertainties in room-temperature line strengths of the CO P(0, 21) and P(1, 21) lines are both 1.5%, respectively, considering the uncertainty range in the corresponding spectral database. This study measured and fitted the line strength of the CO P(0, 37) line, as shown in figure 8(a). The uncertainty in the room-temperature line strength is 4.5% considering 4.0% uncertainty from line-shape fitting and 2.0% uncertainty from data-fitting at elevated temperatures. A 4.0% uncertainty was assumed in the measured absorbance for the selected lines. For the CO P(0, 21)/P(1, 21) line pair, the uncertainties in measured temperature and CO concentration are 3.2% and 6.9%, respectively. For the CO P(0, 21)/P(0, 37) line pair, the uncertainties in measured temperature and CO concentration are 3.1% and 6.4%, respectively. The 4.1% uncertainty in the line shape function (including 0.5% uncertainty in Gaussian line shape, 0.7% uncertainty due to pressure shift, and 0.2% uncertainty due to laser drift) was considered for the two line pairs. The detailed uncertainty analysis is referred to in the previous study [39] (here the profile is shown in supplemental material S4).

Time-resolved temperature measurements were performed in the shock-heated thermal equilibrium mixture (mixture 3), as shown in figure 10. The calculated temperature using T_5, p_5, measured pressure, and isentropic relationship were also shown as a comparison. The shock-heated CO quickly reached a thermal equilibrium state due to the contribution of H_2. Using the two line pairs, the measured temperature fitted well with the calculated temperature in 0–1.4 ms. In addition, the measured data using the P(0, 21)/P(0, 37) line pair showed relatively poor signal-to-noise ratios because of the relatively low temperature sensitivity in the line pair.

Figure 10(b) shows an amplified figure for the reflected-shock-heated region. The calculated temperature reached an equilibrium state by about 8 μs, whereas the measured T_{rot} reached the same state by about 3 μs. The response frequency of the absorption-based thermometry is at least one time faster than that of the pressure transducer.

5.2. Rotational and vibrational temperature measurements for shock-heated thermal non-equilibrium CO

This section presents the simultaneous measurements of time-resolved T_{rot} and T_{vib} for shock-heated thermal non-equilibrium CO/Ar mixture. Figure 11 shows the measured laser signals and pressure profiles in a shock-tube experiment. The laser signals were normalized by the corresponding I_0. Before the arrival of the incident shock, the normalized I_0 signal corresponding to the CO P(0, 21) line is lower than unity due to the strong absorbance of this line at room temperature. With the passage of the incident and reflected shocks, the laser signals corresponding to the CO P(0, 21) and P(0, 37) lines suddenly changed, whereas the laser signal corresponding to the CO P(1, 21) line did not change evidently. After the passage of the reflected shock, all the laser signals changed gradually and reached equilibrium states. During this time, the laser signals corresponding to CO P(0, 21) and P(0, 37) lines were gradually increased, whereas the laser signal corresponding to CO P(1, 21) line was gradually decreased. Corresponding explanations for this phenomenon are shown in the following part.

Figure 12 shows the comparisons of different temperatures during the thermal non-equilibrium processes of the CO/Ar mixture. The measured raw data of these temperatures are shown in supplemental material S5. The black line represents the calculated temperature using T_5, p_5, measured pressure, and isentropic relationship. The pink line represents the measured T_{rot} using CO P(0, 21)/P(0, 37) line pair. The measured T_{rot} suddenly increased after the passage of the shock waves and agreed well with the calculated temperature, indicating that the rotational energy of CO rapidly reached an equilibrium state. In the rotational-equilibrium state, the T_{rot} agreed well with the calculated temperature (black line), which supports the assumption that the translational mode and rotational mode of CO quickly reach an equilibrium state. The measured T_{vib} using CO P(0, 21)/P(1, 21) line pair experienced a relaxation process before reaching the final equilibrium state, as shown by the green line in figure 12. The time histories of the transmitted laser signals in figure 11 are due to the influences of T_{rot} and T_{vib} on the line strengths of the
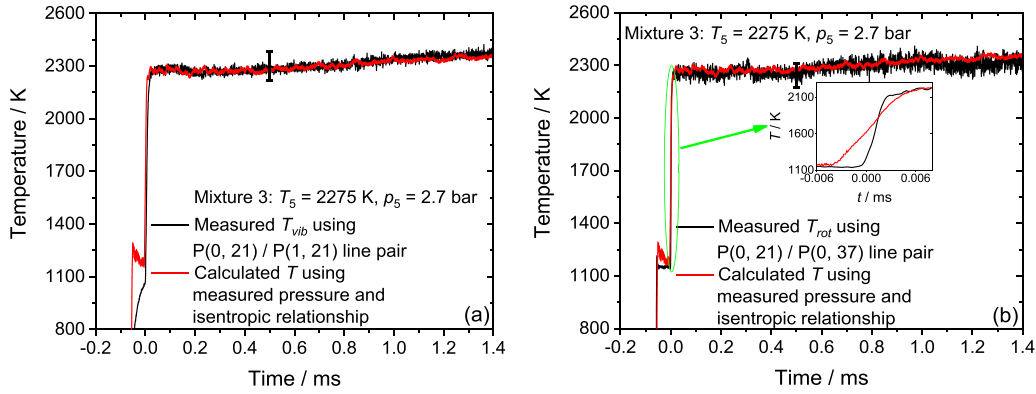
Figure 10. Temperature time-history measurements for shock-heated thermal equilibrium 1.0% CO/2.0% H$_2$/97.0% Ar mixture behind reflected shock waves. (a): P(0, 21)/P(1, 21) line pair. (b): P(0, 21)/P(0, 37) line pair.
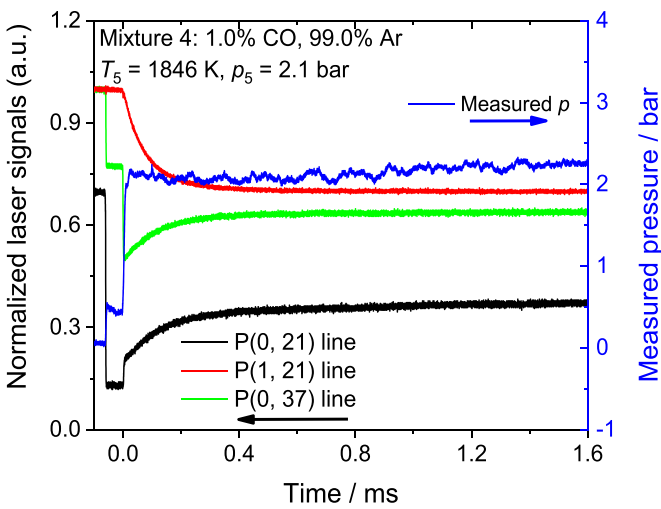

Figure 11. Measured laser signals and pressure profiles for shock-heated thermal non-equilibrium 1.0% CO/99.0% Ar mixture.
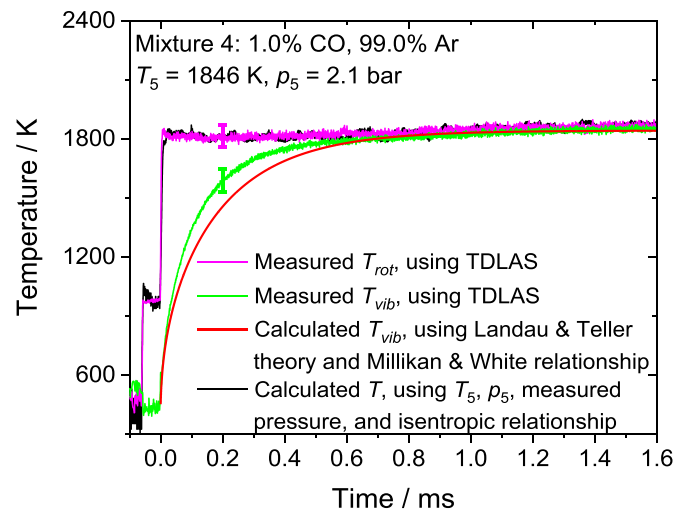

Figure 12. Comparisons of different temperatures for shock-heated thermal non-equilibrium 1.0% CO/99.0% Ar mixture.

selected transition lines, as described by equation (6). Red line represents the calculated T_{vib} using the Landau and Teller theory [42] and Millikan and White relationship [43]. The T_{vib} was calculated from 452 K considering it was pre-excited by the incident shock. The measured and calculated T_{vib} showed similar behaviors, indicating that the Landau and Teller theory [42] well described the time histories of CO vibrational energy (equation (8)). In addition, the measured and calculated T_{vib} agreed well with the equilibrium temperature in the vibrational relaxed state. The measured T_{vib} was slightly faster than the calculated T_{vib}. Future research is suggested to perform state-to-state kinetics simulation on the internal energy conversion of CO.

5.3. Chemical non-equilibrium CO-concentration measurements during the oxidation processes of n-heptane

n-Heptane is one of the alternative fuels for the scramjet [9]. The combustion chamber of the scramjet works at ultra-high temperatures. Therefore, the CO-concentration time-history measurements were performed during the fuel-rich and stoi-chiometric oxidation processes of nC$_7$H$_{16}$/O$_2$/Ar mixtures

over a wide temperature range to show the reaction behaviors of chemical non-equilibrium CO. The CO P(0, 21)/P(1, 21) line pair was selected considering its relatively high temperature sensitivity. The measured data were compared with predictions based on the NUIGMech1.1 [10, 11], the CRECK [12–15] mechanism, and the Liu *et al* [16] mechanism. The measured raw data of CO concentration and pressure profiles are shown in supplemental material S5.

Figure 13 shows the measured and simulated CO-concentration profiles during the fuel-rich oxidation processes of n-heptane at 1510–2750 K and 1.6–2.3 bar. The signal-to-noise ratios in the measured data were poor for the cases with initial temperatures of 2178 and 2743 K due to the weak absorbances and relatively low temperature sensitivity for the line pair at ultra-high temperatures. The CO concentration quickly rises and reaches a plateau at later times. At the rising stage, the predictions using the NUIGMech1.1 [10, 11] and the Liu *et al* [16] mechanism agreed well with the measured data, whereas the CRECK [12–15] mechanism predicted a very fast reaction. In the burnout state, the NUIGMech1.1 [10, 11] and the CRECK [12–15] mechanism well predicted
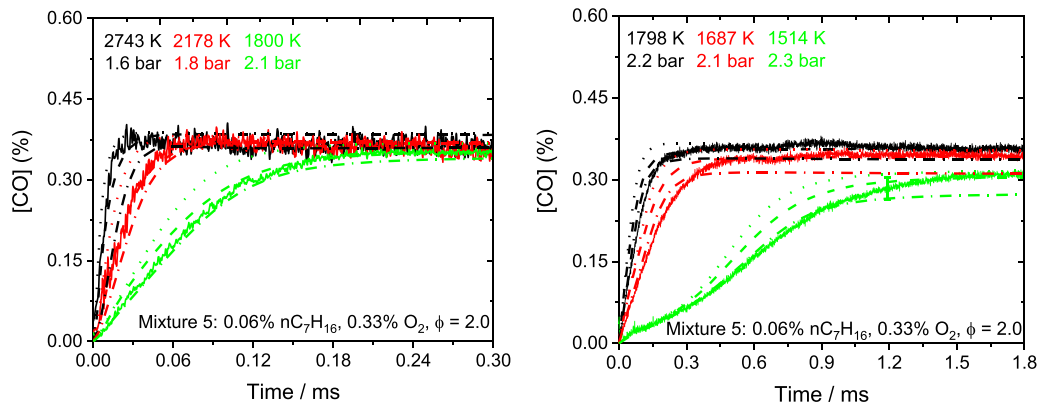
Figure 13. CO-concentration time-history profiles of mixture 5. Solid line: measured data. Dash line: simulations using NUIGMech1.1 [10, 11]. Dot line: simulations using CRECK [12–15] mechanism. Dash dot line: simulations using Liu *et al* [16] mechanism.

Figure 14. CO-concentration time-history profiles of mixture 6. Solid line: measured data. Dash line: simulations using NUIGMech1.1 [10, 11]. Dot line: simulations using CRECK [12–15] mechanism. Dash dot line: simulations using Liu *et al* [16] mechanism.
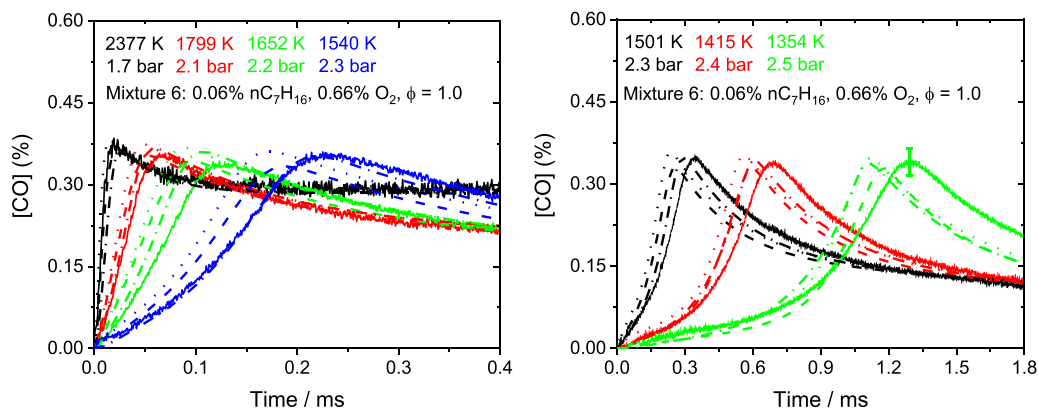
the plateau values of CO concentration, whereas the Liu *et al* [16] mechanism underpredicted the data, especially for the low-temperature cases.

Figure 14 shows the formation and consumption behaviors of CO during the stoichiometric oxidation processes of n-heptane at 1350–2380 K and 1.7–2.5 bar. The selected mechanisms all well predicted the above-mentioned behaviors. At the early stage, the predicted CO concentration agreed well with the measured data. However, at the fast formation/consumption stage, the three mechanisms predicted too-fast reactions for most cases. The NUIGMech1.1 [10, 11] slightly underpredicted the peak values of CO concentration. The interference-free laser-absorption technique showed good flexibility in capturing CO concentration at ultra-high temperatures.

In addition, the high-temperature cases (>2100 K) in figures 13 and 14 show similar CO-formation time scales. It means the oxidation process of n-heptane (mixtures 5 and 6) is insensitive to the increase in the initial temperature at ultra-high temperatures. With the increase of Mach number, the temperature and the flow velocity in the combustion chamber of the scramjet increase simultaneously. The shortened stagnation time in the combustion chamber may cause insufficient combustion considering the temperature insensitivity of fuel reactivity at ultra-high temperatures. Therefore, additional

strategies for increasing fuel reactivity are necessary to ensure successful ignition and fast combustion and to improve energy conversion efficiency.

6. Conclusion

Quantitative measurements of the temperatures in different freedoms during the thermal non-equilibrium processes of CO are prerequisites to studying the non-equilibrium effects of CO and managing the heat transfer during Mars entry. In addition, measurements on the time histories of chemical non-equilibrium CO during fuel combustion at ultra-high temperatures are key prerequisites for summarizing the ignition characteristics and improving the engine performances. The P(0, 21), P(1, 21), and P(0, 37) lines in CO fundamental vibrational band were selected to develop an interference-free laser absorption technique for simultaneous temperature and CO-concentration measurements during the thermo-chemical non-equilibrium processes of CO. The P(0, 21)/P(1, 21) line pair was selected for T_{vib} measurements, whereas the P(0, 21)/P(0, 37) line pair was selected for T_{rot} measurements. The line strengths and collisional broadening coefficients were obtained at 1040–2940 K. Validated experiments at 1050–3010 K and 1.1–2.8 bar showed that the measured

temperature and CO concentration agreed well with the known data.

The time-resolved T_{rot} and T_{vib} were measured during the shock-heated thermal non-equilibrium processes of CO. The technique showed high sensitivity and feasibility in detecting the rotational and vibrational temperatures. The measured T_{rot} rapidly reached an equilibrium state after the arrival of the reflected shock wave and agreed well with the calculated temperature using measured pressure and isentropic relationship. The measured T_{vib} experienced a relaxation process before reaching the final equilibrium state. The measured data showed good agreement with the predictions based on the Landau and Teller theory [42].

Quantitative measurements on the CO-concentration time histories were performed during the oxidation processes of n-heptane over a wide temperature range (1350–2750 K). The measured data showed overall good agreement with the predictions from two detailed mechanisms (NUIGMech 1.1 [10, 11] and CRECK [12–15] mechanism) and one skeletal mechanism (Liu *et al* [16] mechanism). In addition, the reactivity of n-heptane is found to be insensitive to the temperature increase at ultra-high temperatures (>2100 K). Additional strategies are necessary to ensure fast combustion and to improve the energy conversion efficiency for future scramjet.

Data availability statement

All data that support the findings of this study are included within the article (and any supplementary files).

Acknowledgments

ORCID iDs

Dong He ⬤ https://orcid.org/0000-0002-7791-982X
Ting Si ⬤ https://orcid.org/0000-0001-9071-8646

References

[1] Park C, Howe J T, Jaffe R L and Candler G V 1994 Review of chemical-kinetic problems of future NASA missions. II—Mars entries *J. Thermophys. Heat Transfer* **8** 9–23

[2] Johnston C, Brandis A and Sutton K 2012 Shock layer radiation modeling and uncertainty for Mars entry *43rd AIAA Thermophysics Conf.* (American Institute of Aeronautics and Astronautics)

[3] Cruden B A, Prabhu D and Martinez R 2012 Absolute radiation measurement in Venus and mars entry conditions *J. Spacecr. Rockets* **49** 1069–79

[4] Cruden B A, Brandis A M and MacDonald M E 2018 Characterization of CO thermochemistry in incident shockwaves *2018 Joint Thermophysics and Heat Transfer Conf.* (American Institute of Aeronautics and Astronautics)

[5] MacDonald M E, Brandis A M and Cruden B A 2018 Temperature and CO number density measurements in shocked CO and CO_2 via tunable diode laser absorption spectroscopy *2018 Joint Thermophysics and Heat Transfer Conf.* (American Institute of Aeronautics and Astronautics)

[6] Brandis A M, Johnston C O, Cruden B A, Prabhu D K, Wray A A, Liu Y, Schwenke D W and Bose D 2013 Validation of CO 4th positive radiation for Mars entry *J. Quantum Spectrosc. Radiat. Transfer* **121** 91–104

[7] Johnston C O and Brandis A M 2014 Modeling of nonequilibrium CO fourth-positive and CN violet emission in CO_2–N_2 gases *J. Quantum Spectrosc. Radiat. Transfer* **149** 303–17

[8] Urzay J 2018 Supersonic combustion in air-breathing propulsion systems for hypersonic flight *Annu. Rev. Fluid Mech.* **50** 593–627

[9] Colket M B and Spadaccini L J 2001 Scramjet fuels autoignition study *J. Propul Power* **17** 315–23

[10] Wu Y *et al* 2021 Understanding the antagonistic effect of methanol as a component in surrogate fuel models: a case study of methanol/n-heptane mixtures *Combust. Flame* **226** 229–42

[11] El-Sabor Mohamed A A, Panigrahy S, Sahu A B, Bourque G and Curran H J 2021 An experimental and kinetic modeling study of the auto-ignition of natural gas blends containing C1–C7 alkanes *Proc. Combust. Inst.* **38** 365–73

[12] Ranzi E, Frassoldati A, Stagni A, Pelucchi M, Cuoci A and Faravelli T 2014 Reduced kinetic schemes of complex reaction systems: fossil and biomass-derived transportation fuels *Int. J. Chem. Kinet* **46** 512–42

[13] Pelucchi M, Cavallotti C, Faravelli T and Klippenstein S J 2018 H-abstraction reactions by OH, HO_2, O, O_2 and benzyl radical addition to O_2 and their implications for kinetic modelling of toluene oxidation *Phys. Chem. Chem. Phys.* **20** 10607–27

[14] Pelucchi M, Bissoli M, Cavallotti C, Cuoci A, Faravelli T, Frassoldati A, Ranzi E and Stagni A 2014 Improved kinetic model of the low-temperature oxidation of n-heptane *Energy Fuels* **28** 7178–93

[15] Pelucchi M, Cavallotti C, Ranzi E, Frassoldati A and Faravelli T 2016 Relative reactivity of oxygenated fuels: alcohols, aldehydes, ketones, and methyl esters *Energy Fuels* **30** 8665–79

[16] Liu S, Sun T, Zhou L, Jia M, Zhao W and Wei H 2023 A new skeletal kinetic model for methanol/ n-heptane dual fuels under engine-like conditions *Energy* **263** 125648

[17] Blackman V 1956 Vibrational relaxation in oxygen and nitrogen *J. Fluid Mech.* **1** 61–85

[18] Hooker W J and Millikan R C 1963 Shock-tube study of vibrational relaxation in carbon monoxide for the fundamental and first overtone *J. Chem. Phys.* **38** 214–20

[19] Hanson R K and Davidson D F 2014 Recent advances in laser absorption and shock tube methods for studies of combustion chemistry *Prog. Energy Combust. Sci.* **44** 103–14

[20] Goldenstein C S, Spearrin R M, Jeffries J B and Hanson R K 2017 Infrared laser-absorption sensing for combustion gases *Prog. Energy Combust. Sci.* **60** 132–76

[21] He D, Ding Y, Shi L, Zheng D and Peng Z 2021 Simultaneous temperature and CO-concentration time-history measurements during the pyrolysis and ultra-fuel-rich oxidation of ethanol, diethyl ether, n-heptane, and

isooctane behind reflected shock waves *Combust. Flame* **232** 111537

[22] He D, Zheng D, Du Y, Li J, Ding Y and Peng Z 2022 Laser-absorption-spectroscopy-based temperature and NH_3-concentration time-history measurements during the oxidation processes of the shock-heated reacting NH_3/H_2 mixtures *Combust. Flame* **245** 112349

[23] Pineda D I, Bendana F A, Schwarm K K and Spearrin R M 2019 Multi-isotopologue laser absorption spectroscopy of carbon monoxide for high-temperature chemical kinetic studies of fuel mixtures *Combust. Flame* **207** 379–90

[24] Streicher J W, Krish A and Hanson R K 2020 Vibrational relaxation time measurements in shock-heated oxygen and air from 2000 K to 9000 K using ultraviolet laser absorption *Phys. Fluids* **32** 086101

[25] Streicher J W, Krish A, Hanson R K, Hanquist K M, Chaudhry R S and Boyd I D 2020 Shock-tube measurements of coupled vibration–dissociation time-histories and rate parameters in oxygen and argon mixtures from 5000 K to 10 000 K *Phys. Fluids* **32** 076103

[26] Streicher J W, Krish A and Hanson R K 2022 High-temperature vibrational relaxation and decomposition of shock-heated nitric oxide. I. argon dilution from 2200 to 8700 K *Phys. Fluids* **34** 116122

[27] Streicher J W, Krish A and Hanson R K 2022 High-temperature vibrational relaxation and decomposition of shock-heated nitric oxide: II. nitrogen dilution from 1900 to 8200 K *Phys. Fluids* **34** 116123

[28] He D, Shi L, Nativel D, Herzler J, Fikri M and Schulz C 2020 CO-concentration and temperature measurements in reacting CH_4/O_2 mixtures doped with diethyl ether behind reflected shock waves *Combust. Flame* **216** 194–205

[29] Mulvihill C R and Petersen E L 2017 High-temperature argon broadening of CO_2 near 2190 cm^{-1} in a shock tube *Appl. Phys. B* **123** 255

[30] Jelloian C C, Bendana F A, Wei C, Spearrin R M and MacDonald M E 2021 Nonequilibrium vibrational, rotational, and translational thermometry via megahertz laser absorption of CO *J. Thermophys. Heat Transfer* **36** 266–75

[31] He D, Nativel D, Herzler J, Jeffries J B, Fikri M and Schulz C 2020 Laser-based CO concentration and temperature measurements in high-pressure shock-tube studies of n-heptane partial oxidation *Appl. Phys. B* **126** 142

[32] Zheng D, He D, Wang Q-D, Ding Y and Peng Z 2022 Simultaneous measurements of temperature, CO, and CO_2 time-history in reacting n-heptane/O_2/argon mixtures blended with diethyl ether behind reflected shock waves *Combust. Flame* **241** 112057

[33] Spearrin R M, Ren W, Jeffries J B and Hanson R K 2014 Multi-band infrared CO_2 absorption sensor for sensitive temperature and species measurements in high-temperature gases *Appl. Phys. B* **116** 855–65

[34] Spearrin R M, Schultz I A, Jeffries J B and Hanson R K 2014 Laser absorption of nitric oxide for thermometry in high-enthalpy air *Meas. Sci. Technol.* **25** 125103

[35] Cassady S J, Susa A J, Ferris A M, Strand C L and Hanson R K 2019 A two-wavelength ethylene-absorption temperature diagnostic *Meas. Sci. Technol.* **30** 035206

[36] Jelloian C C, Minesi N Q and Spearrin R M 2022 High-speed mid-infrared laser absorption spectroscopy of CO_2 for shock-induced thermal non-equilibrium studies of planetary entry *Appl. Phys. B* **128** 216

[37] Rothman L S, Gordon I E, Barber R J, Dothe H, Gamache R R, Goldman A, Perevalov V I, Tashkun S A and Tennyson J 2010 HITEMP, the high-temperature molecular spectroscopic database *J. Quantum Spectrosc. Radiat. Transfer* **111** 2139–50

[38] Gordon I E *et al* 2022 The HITRAN2020 molecular spectroscopic database *J. Quantum Spectrosc. Radiat. Transfer* **277** 107949

[39] He D, Si T, Fikri M and Luo X 2023 Interference-free laser-based temperature and CO-concentration measurements for shock-heated isooctane and isooctane/ethanol blends *Meas. Sci. Technol.* accepted

[40] Matthews D L 1961 Vibrational relaxation of carbon monoxide in the shock tube *J. Chem. Phys.* **34** 639–42

[41] von Rosenberg C W, Bray K N C and Pratt N H 1971 The effect of water vapor on the vibrational relaxation of CO *Symp. (Int.) Combust.* **13** 89–98

[42] Landau L and Teller E 1936 On the theory of sound dispersion *Phys. Z. Sowjetunion* **10** 34–38

[43] Millikan R C and White D R 1963 Systematics of vibrational relaxation *J. Chem. Phys.* **39** 3209–13

[44] Zhang K, Banyon C, Bugler J, Curran H J, Rodriguez A, Herbinet O, Battin-Leclerc F, B'Chir C and Heufer K A 2016 An updated experimental and kinetic modeling study of n-heptane oxidation *Combust. Flame* **172** 116–35

[45] Zhang K, Banyon C, Burke U, Kukkadapu G, Wagnon S W, Mehl M, Curran H J, Westbrook C K and Pitz W J 2019 An experimental and kinetic modeling study of the oxidation of hexane isomers: developing consistent reaction rate rules for alkanes *Combust. Flame* **206** 123–37

[46] Pineda D I, Bendana F A and Mitchell Spearrin R 2021 Competitive oxidation of methane and C_2 hydrocarbons discerned by isotopic labeling and laser absorption spectroscopy of CO isotopologues in shock-heated mixtures *Combust. Flame* **224** 54–65

[47] Li G, Gordon I E, Rothman L S, Tan Y, Hu S-M, Kassi S, Campargue A and Medvedev E S 2015 Rovibrational line lists for nine isotopologues of the co molecule in the $X^1\Sigma^+$ ground electronic state *Astrophys. J. Suppl. Ser.* **216** 15